Green Chemistry

PAPER

View Article Online
View Journal | View Issue

Cite this: *Green Chem.*, 2025, **27**, 11065

Breaking the C–C coupling barrier in pressurized CO_2RR: local alkalinity control against buffering of CO_2 species at industrial current densities

Shilei Zhang,[a,b] Hang Wang,[a,b] Yang Wang,[a,b] Min Zhang,[a,b] Weimin Wang,[a,b] Liang Zhang,[a,b] Jun Li,[a,b] Xun Zhu,[a,b] Qian Fu *[a,b] and Qiang Liao *[a,b]

Elevating the operating pressure could significantly enhance CO_2 accessibility on the catalyst in electrochemical CO_2 reduction (CO_2RR); however, achieving selective production of multi-carbon (C_{2+}) products under pressurized conditions remains a critical challenge because elevated pressure could shift the selectivity towards C_1 products. This work systemically investigated the variation of product selectivity induced by pressure and electrolyte composition, and demonstrates that a local pH drop induced by increased pressure is the key reason for hindered C–C coupling, as confirmed by *in situ* Raman and multi-physics simulation. The elevated pressure results in an increase of the electrolyte's buffering capacity, which neutralizes the alkaline microenvironment near the catalyst, thereby impeding the C–C coupling. Decreasing the buffering ability (using non-buffered KCl electrolyte) or increasing the current density (from 0.4 A cm^{-2} to 1.0 A cm^{-2}) could maintain a high interfacial alkalinity under elevated pressure, promoting C–C coupling. By mapping pressure–current density operational windows, the optimal conditions were identified, achieving 70% C_2 faradaic efficiency (50% for C_2H_4) at 5 bar and 1 A cm^{-2}, demonstrating superior C_2 product selectivity. This work establishes electrolyte engineering principles for industrial CO_2RR, enabling carbon-neutral chemical production under practical pressurized conditions through microenvironmental regulation.

Received 11th May 2025,
Accepted 7th August 2025

DOI: 10.1039/d5gc02334c

rsc.li/greenchem

Green foundation

1. This study presents a pressurized liquid-phase electrolyzer that enables high-rate conversion of CO_2 to value-added C_2 chemicals under industrial conditions. This technology offers an alternative route for scalable CO_2 utilization and facilitates green chemical synthesis by replacing fossil fuel-derived feedstocks.
2. The proposed electrolyzer achieves 70% faradaic efficiency (FE) for C_2 products at 5 bar, with 50% selectivity towards ethylene. It attains a C_2 partial current density of 724 mA cm^{-2}, outperforming ambient-pressure benchmarks by 10 fold.
3. Future work will focus on scaling up the electrolyzers (including their key components) and enhancing the energy conversion efficiency of the proposed system.

1. Introduction

Electrochemical CO_2 reduction (CO_2RR) to value-added products, such as ethylene (C_2H_4) and ethanol (EtOH), represents a pivotal route toward carbon neutrality.[1] Currently, gas-fed membrane electrode assembly (MEA) cells with gas diffusion electrodes (GDEs) are widely employed for CO_2RR, aiming to address the current density limitation caused by the low solubility of CO_2 (~33 mM under ambient conditions).[2] Notably, during the CO_2RR process, the generated OH^- reacts with CO_2 and forms (bi)carbonate (*e.g.*, $2CO_2 + 8H_2O + 12e^- \rightarrow C_2H_4 + 12OH^-$, $CO_2 + OH^- \rightarrow HCO_3^-$), which accumulates in the GDEs and blocks the reactant transport channels, leading to performance degradation.[3–5]

Although some studies applied flowing water to wash the cathode and remove salts from the reaction zone,[6,7] this approach substantially increases the operational complexity. On the other hand, directly using cathodes immersed in flowing electrolyte and using dissolved CO_2 species as

[a]*Key Laboratory of Low-grade Energy Utilization Technologies and Systems, Ministry of Education, Chongqing University, Chongqing 400044, China.*
E-mail: fuqian@cqu.edu.cn, lqzx@cqu.edu.cn; Fax: +8623 65102474; Tel: +86 23 65102474
[b]*Institute of Engineering Thermophysics, School of Energy and Power Engineering, Chongqing University, Chongqing 400044, China*

reactants could essentially mitigate salt precipitation issues and avoid the extra washing procedure. The primary challenge stems from the limited accessibility of CO_2 in the dissolved phase,[8,9] which leads to significant side reactions (HER: $2H_2O + 2e^- \rightarrow H_2 + 2OH^-$), particularly at high current densities. Notably, enhancing the partial pressure of CO_2 can significantly enhance the CO_2 solubility,[10,11] increase the CO_2 coverage on the catalyst surface,[12] and accelerate the reaction kinetics,[13] thereby greatly improving the CO_2RR performance. For example, Lamaison *et al.* carried out CO_2RR on a Zn–Ag catalyst at 9.5 bar, demonstrating the enhanced mass transfer ability induced by pressure and achieving a selectivity of 72% for CO at a high current density of 0.4 A cm^{-2}.[14] In addition, pressurized CO_2RR shows high compatibility with industrial CO_2 capture processes (*e.g.*, high-pressure water scrubbing, pressure swing adsorption), avoiding the energy-wasteful process of CO_2 decompression steps.[15,16] Therefore, CO_2RR using dissolved CO_2 at elevated pressures is a promising approach for industrial-scale applications.

However, the selective synthesis of multi-carbon (C_{2+}) products remains a significant challenge under pressurized conditions. Current studies reveal that Cu-based catalysts under high CO_2 pressures exhibit formate-selective behavior due to the CO_2 coverage-driven elevation of *OCHO intermediate adsorption energy barriers.[17,18] While the majority of research emphasizes intermediate transformations, the variation of electrolyte contents induced by elevated CO_2 concentrations (*e.g.*, 1 bar CO_2 in pure water, leading to pH ≈ 3.95) and its effect on CO_2RR remain underexplored. Maintaining an alkaline interfacial pH (>10) is widely recognized as essential for facilitating C–C coupling *via* enhanced *CO dimerization.[19–21] However, neutral and acidic electrolytes would boost the coupled proton–electron transfer step, enhancing C_1 production (*e.g.*, HCOOH, CH_4).[22–24] Under pressurized conditions, the dissolved CO_2 would generate bicarbonate and H^+, buffering the generated OH^- during CO_2RR (*e.g.*, $HCO_3^- + OH^- \rightarrow H_2O + CO_3^{2-}$), creating an unfavorable microenvironment for C–C coupling.[25–27] This unresolved conflict between pressure-enhanced mass transfer and pH-governed selectivity constitutes the key bottleneck for industrial-scale C_{2+} production.

In this work, we aim to achieve high rates of C_2 production with the assistance of elevated pressure, proposing a strategy to minimize the pH decay through electrolyte design and pressure–current adaptation. By comparing a buffering electrolyte ($KHCO_3$) and a non-buffering electrolyte (KCl), we demonstrate the significant influence of the buffering ability of electrolytes on C_2 production selectivity. Complemented by multi-physics simulation and *operando* Raman spectroscopy at a wide range of current densities (0.2–1.0 A cm^{-2}), we validate that C_2 production performance is in accordance with the CO_2 concentration-dependent modulation of interfacial OH^- distribution. Besides, modifications of the applied current density on the interfacial OH^- were quantitatively studied. Through optimizing the current density window at elevated pressures, we simultaneously regulated the local CO_2 concentration and interfacial pH, achieving enhanced C_2H_4 current density and selectivity. As a result, the system achieved record high current densities of 554 mA cm^{-2} for C_2H_4 and 724 mA cm^{-2} for total C_2 products, exceeding 70% FE for C_2 production at 1.0 A cm^{-2}. This work underscores interfacial pH management and microenvironment control as critical factors for pressurized CO_2RR toward industrial application.

2. Methods

2.1 Chemicals and materials

Copper mesh (100 mesh, 99.9%) was purchased from Jiangxin Metal Co. Ltd (Hebei, China). Sodium hydroxide (NaOH, 99.9%) and ammonium persulfate ($(NH_4)_2S_2O_8$, 98%) were purchased from Aladdin Company (Shanghai, China). HCl (36 wt%), acetone, and EtOH were purchased from Chuandong Chemical Group (Chongqing, China).

2.2 Synthesis of the CuNNA electrode

The CuNNA catalysts were prepared *via* chemical etching of a 100 mesh Cu mesh woven with 100 μm Cu fibers. The etching solution consisted of 24 g of NaOH, 11.41 g of $(NH_4)_2S_2O_8$, and 500 mL of ultra-pure water. The raw Cu mesh was sequentially washed with HCl (36 wt%), acetone, EtOH, and water. After blow-drying under N_2, the Cu mesh was immediately immersed in the etching solution for 15 min at 5 °C. After etching, $Cu(OH)_2$ nanoneedle arrays were successfully formed on the smooth surface of the Cu fiber. In the following process, the as-prepared Cu mesh was dehydrated to CuO at 180 °C for 60 min under an air atmosphere. The loading of the catalyst (CuO nanoneedles) was determined *via* acid washing and found to range from 1 to 1.2 mg cm^{-2}.

2.3 Material characterization

The morphology of the CuNNA catalyst was studied by field emission scanning electron microscopy (FE-SEM) (Quattro S, ThermoFisher Scientific, USA) and high-resolution transmission electron microscopy(HRTEM) (Talos F200S, ThermoFisher Scientific, USA). All length measurements and filtering processes were performed using the Digital Micrograph software.

X-ray diffraction (XRD) was carried out on a BRUKER D8 XRD system (BRUKER Company, Germany) equipped with a Co Kα source over a range from 10° to 90°. The X-ray photoelectron spectroscopy (XPS) results were acquired using a ThermoFisher ESCALAB 250Xi spectrometer (ThermoFisher Scientific, USA).

2.4 Electrochemical evaluation of CO_2RR performance

H-cell electrochemical tests were carried out with an electrochemical workstation (PMC-200, Ametek, America). The catalytic performance was evaluated in a gas-tight three-electrode H-type cell, which included two chambers separated by an UltrexCMI-7000 membrane (Membranes International Inc., Ringwood, NJ, USA). The working electrodes were cut into 1 ×

1 cm^2 sections. The counter electrode was Pt foil, and the reference electrode was Ag/AgCl (filled with saturated KCl solution). Before the test, 60 mL of electrolyte was added to both chambers of the H-type cell. To obtain the CO_2 saturated electrolyte, the electrolyte was continuously sparged with CO_2 gas (99.999%) with a flow rate of 30 standard cubic centimeters per minute (sccm) for 30 minutes. Before electrolysis, the CuO NNA was reduced in 0.5 M KCl or 0.5 M $KHCO_3$ at −1.8 V (*vs.* Ag/AgCl) until the current became stable. All potentials obtained were converted to a reversible hydrogen electrode (RHE) according to E (*vs.* RHE) = E (*vs.* Ag/AgCl) + 0.197 + 0.0591 × pH, except for the reducing potential which was annotated.

Liquid MEA tests were carried out in an MEA cell, in which 1 M KOH was used as the anolyte and the catholyte saturated with CO_2 was injected into the cathode at a flow rate of 60 mL min^{-1}. Nickel foam was used as the anode. A Nafion 115 membrane (DuPont, USA) was used to separate the chambers. All gas products were analyzed using a gas chromatograph (8890, Agilent Technologies, Santa Clara, CA, USA). The faradaic efficiency was calculated according to eqn (1) taking CO as an example:

$$FE_{CO} = \frac{I_{CO}}{I} = \frac{xvnF/V_m}{It}. \quad (1)$$

In the equation, I_{CO} is the partial current of CO (A), I is the total current obtained at the constant potential tests or the value set for chronopotentiometry in L-MEA tests (A), x is the CO ratio obtained from the gas chromatograph, v is the total gas volume, n is the electron number consumed for every CO_2 molecule (n = 2 for $CO_2 \rightarrow CO$ and $HCOO^-$; n = 8 for $CO_2 \rightarrow CH_4$; n = 12 for $2CO_2 \rightarrow C_2H_4$ and C_2H_5OH), F is the faradaic constant (96 485 C mol^{-1}), V_m is the molar volume at 298 K (24.5 L mol^{-1}), t is the test time (s), and Q is the total charge consumed in the test (C).

The liquid products were analyzed using a ^1H nuclear magnetic resonance (NMR) spectrometer (Bruker Avance 400 dir) with DMSO (Sigma-Aldrich, ≥99.5%) as an internal standard. The ^1H NMR spectra were collected at ambient temperature, operating at 400 MHz for ^1H nuclei under water suppression mode. The water signal was suppressed using the Watergate W5 pulse sequence with double gradient echoes. Using this method, we determined the concentration of the liquid products in the catholyte solution and calculated the total FE of liquid products. The FE was calculated according to eqn (2) taking $HCOO^-$ as an example:

$$FE_{HCOO^-} = \frac{I_{HCOO^-}}{I} = \frac{xvnF}{It} \quad (2)$$

In the equation, x is the molar concentration of the $HCOO^-$ and v indicates the electrolyte volume.

2.5 *In situ*/*operando* Raman experiments

The *in situ* Raman spectra were obtained using a LabRAM HR Evolution (HORIBA Jobin Yvon S.A.S.) confocal Raman microscope with a 532 nm laser. An objective with a long working distance (Leica Microsystems, ×50) was used. A typical cell designed for Raman (Gaoss Union, C031-2) was used for the tests. The H-cell was equipped with a reference electrode (Ag/AgCl, filled with saturated KCl solution), a counter electrode (Pt wire) and a working electrode. The acquisition time was 30 s for the steady-state experiments at different potentials. The optical grating was 600 g per mm.

The *operando* Raman experiment was carried out on a custom-made cell equipped with an optical window made of sapphire glass under a wide range of current densities (0–1 A cm^{-2}). The flow rate and back pressure were set the same as in the CO_2RR process.

2.6 Computational method

A numerical model was established to simulate the local pH using the COMSOL Multiphysics software. The system was modeled in one-dimension (1D). The thickness of the diffusion layer was assumed to be 50 μm.[17,18] A porosity (ε) of 60% and a length of the catalyst of 300 nm layer ($L_{catalyst}$) were considered in the model. The right boundary represents the bulk electrolyte, as shown in Fig. S4. All the interactions between the species in the electrolyte (CO_2, HCO_3^-, CO_3^{2-}, OH^-, H^+, products, and H_2O) were considered. Henry's law and the Sechenov equation were used to calculate the CO_2 concentration. The model involves CO_2RR, aqueous carbonate equilibria, and dissolved species transport in liquids. Full mathematical formulations of the governing equations (*e.g.*, mass conservation, charge balance) and parameter tables (*e.g.*, diffusion coefficients, rate constants) are provided in the SI.

3. Results and discussion

3.1 Synthesis and characterization of Cu NNA catalysts

The Cu nanoneedle array (NNA) catalysts were synthesized through a three-step process involving chemical etching, thermal treatment, and *in situ* electrochemical reduction (Fig. S1). Initial etching of copper wires generated uniform Cu $(OH)_2$ nanoneedle arrays, which were subsequently converted to CuO *via* thermal dehydration, forming a deep brown mesh. The scanning electron microscopy (SEM) characterization (Fig. S6 and Fig. 1c) revealed that the hierarchical NNA architecture maintained structural integrity throughout the processing, exhibiting 5 μm-long needles with sharp tips. These morphological features are known to enhance local electric fields and elevate the potassium ion concentration,[28] which could suppress the HER under acidic conditions.[8,29]

Previous works demonstrated that halide ions play a significant role in the modification of the catalyst structure and valence state through specific adsorption, which must be carefully considered.[23,30] To avoid structure reconstruction differences in different electrolytes, 0.5 M KI was added to the electrolyte in L-MEA tests.[31,32] Transmission electron microscopy (TEM) analysis was carried out on the Cu NNA after CO_2RR (0.6 A cm^{-2}, 5 bar for 15 min for all post-mortem samples) in $KHCO_3$ and KCl electrolytes. The TEM images (Fig. 1d and

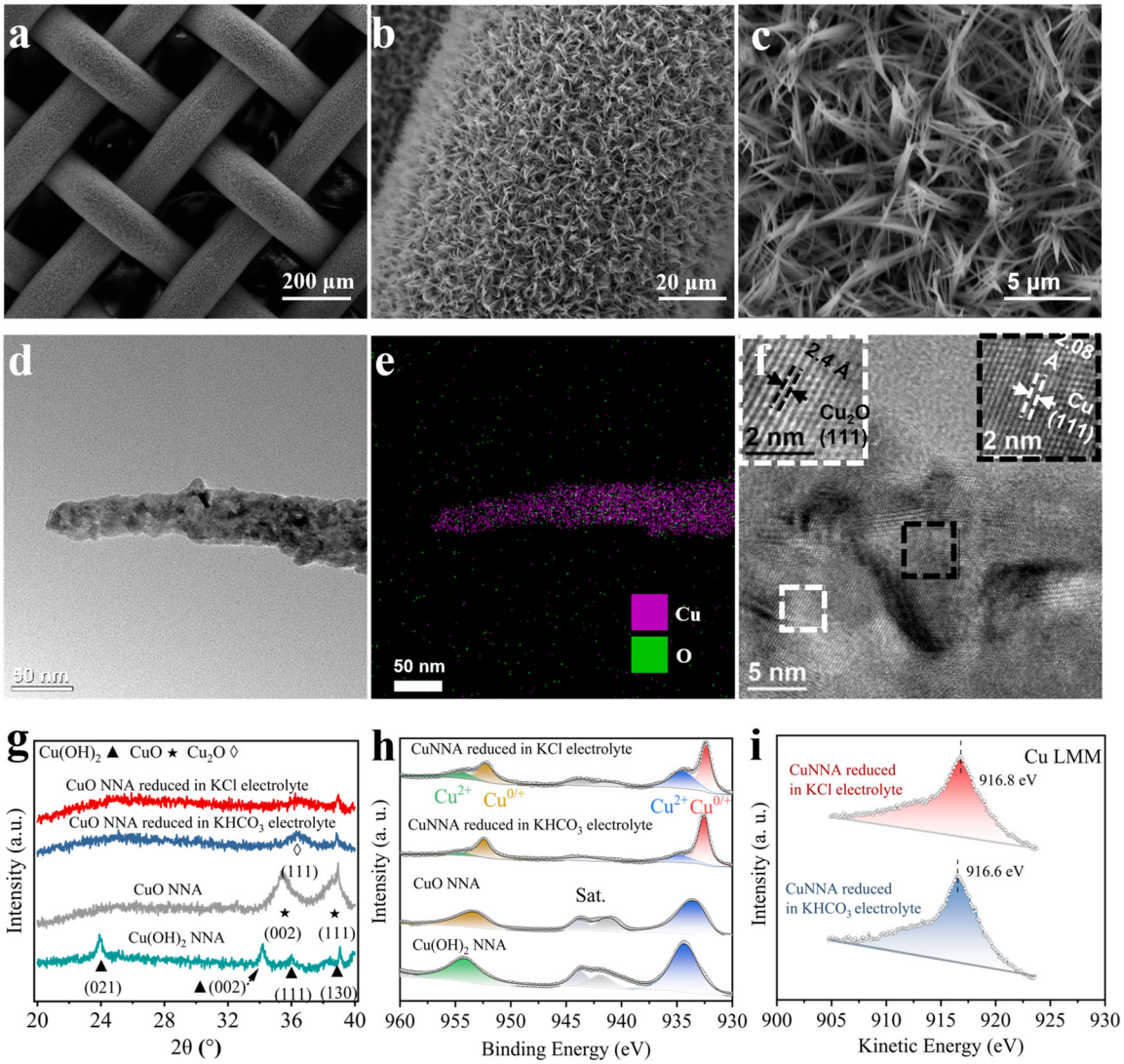

Fig. 1 (a–c) SEM images of the Cu NNA catalyst; (d) TEM images, (e) elemental mapping, (f) high resolution TEM of the Cu NNA catalyst after CO_2RR in $KHCO_3$ electrolyte; (g) XRD spectrogram, (h) XPS spectrogram of Cu 2p spectrogram for $Cu(OH)_2$, Cu NNA, and CuNNA after *in situ* reduction; (i) Cu LMM spectrogram of the Cu NNA catalyst reduced in KCl and $KHCO_3$ electrolytes.

Fig. S7a) reveal similar needle-like structures in both samples, with an average diameter of approximately 50 nm at the base and gradually tapering towards the tip. Elemental distribution (Fig. 1e and Fig. S7b) of the reduced Cu NNA demonstrated homogeneous Cu/O distribution across both $KHCO_3$- and KCl-reduced samples. The morphologies and elemental distributions of Cu NNA reduced in the different electrolytes are similar, which ensures that the performance in the two electrolytes will not be affected by structure reconstruction and valence state variation.

X-ray diffraction (XRD) was carried out to identify the species and crystal patterns. All samples delivered strong Cu (PDF#04-0836) peaks (Fig. S8), which represent the backbone of the Cu mesh. After the thermal treatment, $Cu(OH)_2$ (PDF#13-0420) was fully dehydrated to CuO (PDF#45-0937), which mainly consists of CuO (002) and (111) facets (Fig. 1g). The characteristic Cu_2O (PDF#05-0667) peak confirms the preservation of Cu^+ species in both the $KHCO_3$- and KCl-reduced samples, as evidenced by X-ray diffraction analysis. The X-ray photoelectron spectroscopy (XPS) analyses (Fig. 1h) suggest that the precursor exhibits distinct Cu^{2+} features with a strong satellite peak and a higher binding energy of Cu 2p. Samples reduced in KCl electrolyte show a slightly higher $Cu^{2+}/Cu^{0/+}$ ratio than that of Cu NNA reduced in $KHCO_3$ electrolyte, indicating that a slightly more Cu^{2+} sites are preserved in the samples reduced in KCl electrolyte. The Cu^0 and the Cu^+ species were identified from the Cu Auger LMM transition spectrum (Fig. 1i). An intense peak for Cu^+ species (~916.6 eV) was detected in CuNNA reduced in $KHCO_3$ electrolyte, whereas a 0.2 eV positive shift (~916.8 eV) was observed in CuNNA reduced in KCl electrolyte. This Cl^--induced chemical shift suggests potential Cu–Cl coordination.[33–35] Given that the

additive (KI) could more efficiently stabilize the Cu oxidation state,[31,32] the impact of the small amount of Cu–Cl coordination on the catalytic performance is negligible. This comprehensive characterization confirms that the KI-stabilized Cu NNA maintains structural and chemical consistency across electrolytes, enabling isolated study of pH effects without interference from morphological or valence state variations.

3.2 Pressurized CO_2RR in liquid-flow MEA cells

To mitigate the mass transfer limitation in H-cells,[12,13,18] a custom-made liquid-flow MEA cell system was established, which takes dissolved CO_2 as the reactant. As illustrated in Fig. 2a, a pressurized electrolyte reservoir is connected to the CO_2 cylinder for CO_2 supply and maintains the elevated pressure. Adopting this system, CO_2RR performance testing was conducted at varied current densities and pressures using the CuNNA catalyst.

Initially, a current density of 0.4 A cm^{-2} was applied to assess the influence of pressure on the electrochemical performance. Fig. 2b shows the results obtained in the 1.5 M $KHCO_3$ electrolyte (all subsequent experiments using $KHCO_3$ electrolyte were conducted with 1.5 M $KHCO_3$/0.5 M KI unless otherwise specified). Under ambient pressure (1 atm), the HER dominated the reaction and the FE for total CO_2RR products was only 13.6%. As the operating pressure increased, the FE for total CO_2RR products gradually increased due to the elevated concentration of the reactant (CO_2) near the electrode surface.[10,17,18] At 4 bar CO_2 pressure, the FE for total CO_2RR products reached 53.8%. Notably, the $FE_{C_2H_4}$ value increases from 5.2% to 19.3%, representing a fourfold increase. However, H_2 is still the major product, accounting for approximately 40% at 0.4 A cm^{-2} and 4 bar.

Motivated by the excellent performance of KCl electrolyte achieved in similar electrochemical systems,[36–38] we evaluated the performance using 1.5 M KCl as the non-buffering catholyte (all subsequent experiments using KCl electrolyte were conducted with 1.5 M KCl/0.5 M KI unless otherwise specified). As shown in Fig. 2c, the FE value for total CO_2RR products in KCl electrolyte (48.3%) shows a nine-fold increase compared to that in $KHCO_3$ electrolyte (5.2%) under ambient pressure. When the operating pressure was increased to 2 bar, the FE_{CO_2RR} value in KCl electrolyte significantly increased to 80.8%, and the dominant product shifted from H_2 to C_2H_4 (40%). However, as the pressure further increased from 2 bar to 4 bar, the $FE_{C_2H_4}$ started to decline as well as the overall FE for CO_2RR in KCl electrolyte. On the other hand, the performance in $KHCO_3$ electrolyte maintained a positive correlation between FE_{CO_2RR} and pressure (1–4 bar), and KCl exhibited volcano-type dependence peaking at 2 bar. The different trends in buffering electrolyte and non-buffering electrolyte are consistent with the change in electrolyte composition induced by CO_2 pressurization, with the acidification induced by pressurization being more severe in non-buffering electrolyte than in buffering electrolyte (Tables S2 and S3).

Furthermore, the product distribution analysis revealed a significant pressure-dependent selectivity shift in KCl electrolyte systems. As illustrated in Fig. 2d, the ratio of C_2 production to C_1 production (C_2/C_1) exhibits significant growth from 0.8 (1

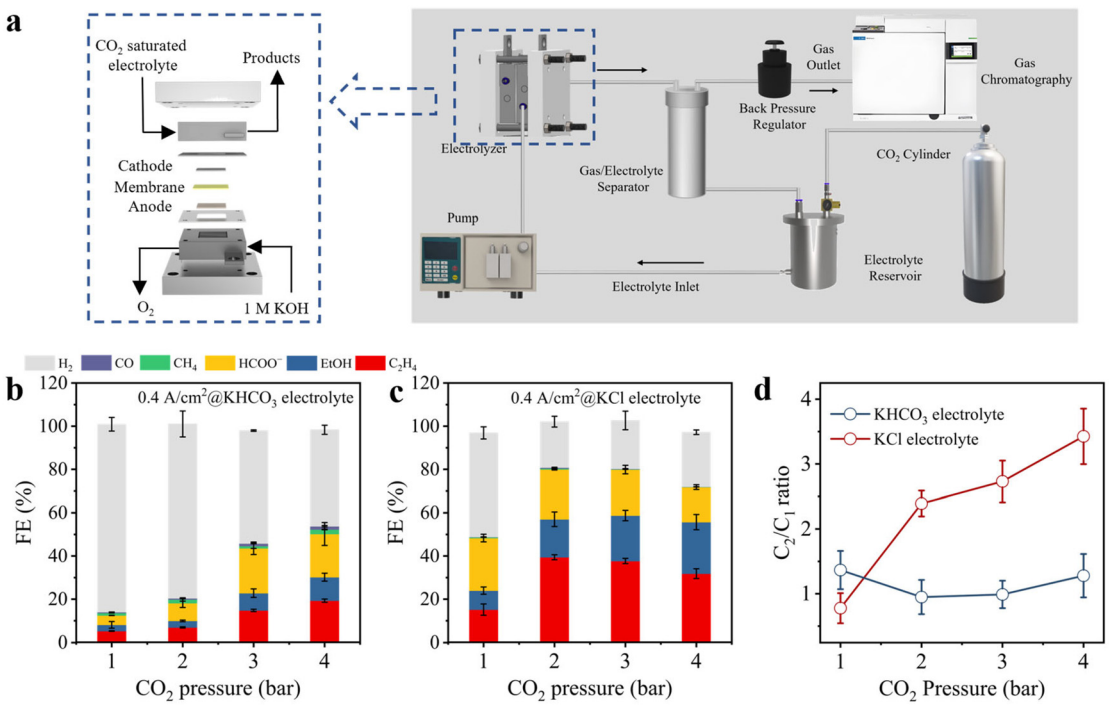

Fig. 2 (a) Illustration of the L-MEA cells (left) and the system schematic for pressurized CO_2RR (right); (b) the FE of Cu NNAs in $KHCO_3$ electrolyte under 0.4 A cm^{-2} and different pressures; (c) the FE of Cu NNAs in KCl electrolyte under 0.4 A cm^{-2} and different pressures; (d) the FE_{C_2}/FE_{C_1} ratio as a function of applied pressure.

bar) to 3.4 (4 bar) under KCl conditions, representing a 325% enhancement. In the $KHCO_3$ systems, the C_2/C_1 ratio maintains a constant value of 0.9–1.1 across the same pressure range. The selectivity difference in the two electrolytes demonstrates that the intrinsic activity of the catalyst in the two electrolytes undergoes significant transition through intermediate modulation.[39,40]

3.3 Local pH variation induced by pressure and CO_2 electroreduction

To evaluate the influence of electrolytes on the intrinsic activity of the CuNNA catalyst, H-cell experiments were conducted under ambient conditions (Fig. 3a–c). In 0.5 M $KHCO_3$ electrolyte, the HER dominated the reaction, with FE_{H_2} showing a positive correlation with the applied potential (Fig. 3a). Remarkably, C_2H_4 was still the major CO_2RR product, demonstrating that the nanoneedle structure effectively promotes C–C coupling.[41] At −1.2 V, a $FE_{C_2H_4}$ value of 23.2% was obtained, which is significantly higher than those for FE_{CO} (1.8%) and FE_{CH_4} (3.1%). As the potential became more negative, the $FE_{C_2H_4}$ value started to decline with an increase of FE_{CH_4}. At all potentials in the range, the FE_{CO} value decreased with an increase in the potential. Thus, the mechanism of C_2 production predominated in the CO dimer ($2{*}CO + e^- \rightarrow {*}OCCO^-$).[40] In KCl electrolyte (Fig. 3b), the FE_{H_2} was markedly suppressed compared to that in $KHCO_3$ electrolyte, decreasing within the range of −0.9 V to −1.4 V. The lowest FE_{H_2} (19.4%) and the highest $FE_{C_2H_4}$ (45.5%) were at −1.35 V. The $FE_{C_2H_4}$, FE_{CH_4} and FE_{CO} values exhibited similar trends in the two electrolytes, which suggests that the C_2 production mechanism in KCl electrolyte is the same as that in $KHCO_3$ electrolyte. To further assess the C_2H_4 production efficiency, the partial current density of C_2H_4 ($j_{C_2H_4}$) is compared in Fig. 3c. The highest $j_{C_2H_4}$ in KCl (50.4 mA cm^{-2}) was twofold higher than that in $KHCO_3$ (24.8 mA cm^{-2}).

The performance enhancement further reveals the modification of Cl^- with the intrinsic activity of the Cu catalyst. To gain insights into this mechanism, *in situ* Raman spectroscopy was carried out to reveal the detailed spectra of intermediate vibrations induced by KCl electrolyte.[42] As shown in Fig. 3c, distinct peaks for adsorbed CO (*CO) can be observed in the range 2000–2200 cm^{-1}. Peak fitting and deconvolution at this range yields a low-frequency band (LFB) at ~2055 cm^{-1} and a high-frequency band (HFB) at ~2115 cm^{-1}, which can be attributed to *CO intermediates adsorbed on terrace and step sites, respectively.[29,39,43,44] In addition, another broad band at a lower Raman shift of ~1940 cm^{-1} was observed, which arises from the interaction between *CO intermediates.[39,45]

The LFB *CO peak remains near constant as the potential increases, while the HFB *CO peak exhibits potential-dependence. The HFB *CO intensity increases from −0.3 to −0.5 V, indicating its accumulation at lower potentials. At higher potentials (more negative than −0.5 V), the HFB *CO intensity starts to decline, likely due to its consumption in CO–CO coupling and C_{2+} production. Thus, HFB *CO is the preferred reactive intermediate for C–C coupling. In contrast, LFB *CO occupies Cu surface sites, showing limited contribution to C_{2+} production. The high percentage of HFB in total *CO, as depicted in Fig. 3d, confirms that KCl electrolyte promotes the formation of active HFB *CO. In $KHCO_3$ electrolyte, however, LFB *CO dominates, increasing the C–C coupling barrier and exacerbating HER side reactions.[39] Besides the intermediate

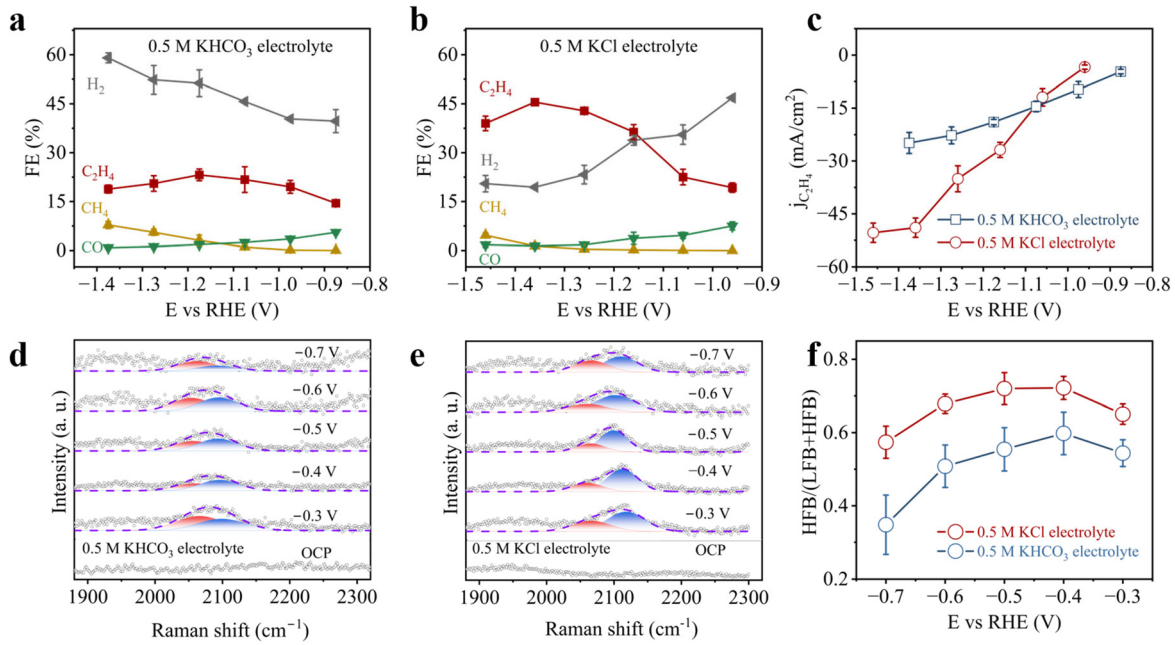

Fig. 3 Electrochemical CO_2 reduction performances in the H-cell and *in situ* Raman spectroscopy. FE of gaseous products at different potentials in (a) 0.5 M $KHCO_3$, (b) 0.5 M KCl; (c) $j_{C_2H_4}$ in 0.5 M $KHCO_3$ and 0.5 M KCl; the *in situ* Raman spectrum obtained in (d) 0.5 M $KHCO_3$ electrolyte and (e) 0.5 M KCl electrolyte; (f) the ratio of HFB in the total *CO (LFB + HFB).

change, the bicarbonate/carbonate composition on the electrode is quite different in the two electrolytes, suggesting distinct differences in the local pH of the electrodes.

To accurately access the bicarbonate/carbonate composition in the two electrolytes within L-MEA cells, we conducted *operando* Raman studies based on a custom-designed MEA cell with an optical window (Fig. 4a). Recent works demonstrate that *in situ* pH microelectrodes[46] and fluorescence[47] can obtain an accurate pH near the electrode, yet *operando* Raman[48–50] spectroscopy shows better compatibility with the pressurized MEA. This setup enables the real time acquisition of Cu_2O and bicarbonate/carbonate Raman signals under conditions of 4 bar CO_2 pressure and 0.2–1.0 A cm^{-2}, as shown in Fig. 4b and c. The obvious signals of Cu_2O (417 cm^{-1}) prove that the Cu^+ species remains stable during the electrolysis, which could be ascribed to the KI additive. The *operando* Raman spectroscopy reveals distinct interfacial pH environments in the two electrolytes. In $KHCO_3$ electrolyte, a high bicarbonate concentration on the interface was observed. At current densities exceeding 0.4 A cm^{-2}, a weak peak corresponding to carbonate (ν = 1058 cm^{-1}) emerged. However, in KCl electrolyte, carbonate is the main species on the interface with a weak bicarbonate peak at OCP. In $KHCO_3$ electrolyte, the weak carbonate peak indicates a weakly alkaline interface, which is unfavorable for C–C coupling.[49] Through ionization equilibrium, it can be deduced that the interface pH is much higher in KCl electrolyte than in $KHCO_3$.

The chemical reactions at the interface, shown in Fig. 4d, are critical for elucidating the local pH dynamics. During the dissolution of CO_2, the electrolyte is acidified and the concentration of bicarbonate increases (Eq_1). The high concentration of bicarbonate could inhibit the acidification but neutralize the CO_2RR generated OH^- (Eq_2) as shown in Eq_3. To quantify the pH balance in the bulk electrolyte and local interface, we conducted a multiphysics simulation based on the reactions and diffusion. The simulated data (Fig. S18) illustrate the concentration ratio of carbonate and bicarbonate in the bulk and the interface in the two electrolytes at 4 bar. It agrees well with the Raman result that little carbonate exists on the interface of the electrode in $KHCO_3$ electrolyte and the opposite trend is seen in KCl electrolyte.

Based on this model, we further investigate the influence of pressure on the interface chemical environment. In $KHCO_3$ electrolyte, the influence of pressure on the interface pH is subtle (Fig. 4e). Notably, increasing the pressure significantly reduces the surface OH^- concentration in KCl electrolyte (Fig. 4f). As the pressure increases from 2 to 4 bar, the interfacial OH^- concentration decreases from 33.8 mM to 23.0 mM. This reduction in alkalinity explains the decline in performance at 0.4 A cm^{-2} between 2 and 4 bar in KCl electrolyte. Moreover, the interface pH continues to decrease as the pressure increases from 4 to 5 bar. This can be attributed to the increasing amounts of H^+, dissolved CO_2, and bicarbonate generated during pressurization, which would neutralize the local alkaline environment and impede the C–C coupling. In summary, while the CO_2 pressure can enhance the CO_2RR performance, it also lowers the interface pH, leading to a performance decrease above certain pressures. At a current density of

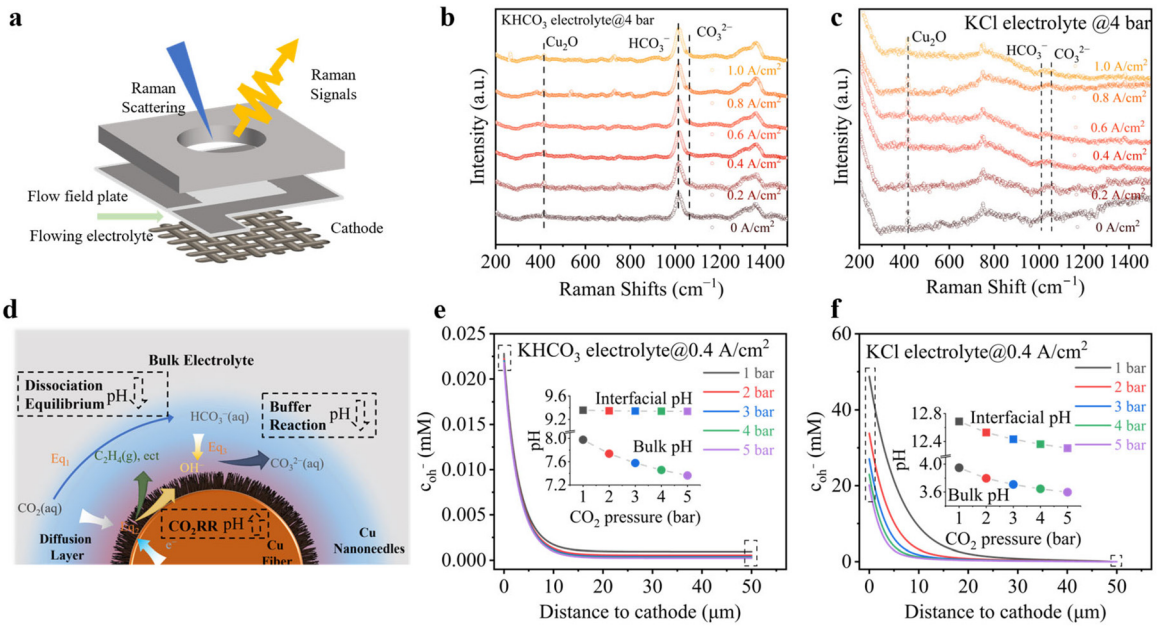

Fig. 4 (a) Illustration of *operando* Raman setup based on an L-MEA cell; *operando* Raman spectrum obtained in (b) $KHCO_3$ electrolyte and (c) KCl electrolyte; (d) illustration of reactions occurring on the cathode in the L-MEA cell; COMSOL simulated OH^- concentration as a function of distance to the cathode in (e) $KHCO_3$ electrolyte and (f) KCl electrolyte.

0.4 A cm^{-2} and CO_2 pressures exceeding 2 bar, the diminished pH begins to inhibit CO_2RR performance.

3.4 Optimization of C–C coupling in KCl electrolyte

Motivated by local pH variation induced by the CO_2RR process and buffer reactions, we further evaluated the $FE_{C_2H_4}$ across a broad range of current densities (0.2–1.0 A cm^{-2}) and CO_2 pressures (1–5 bar) in the two electrolytes ($KHCO_3$ and KCl) to optimize ethylene production. Fig. 5a and c reveal distinct pressure-dependent performance enhancements in these electrolyte systems. In $KHCO_3$ electrolyte, $FE_{C_2H_4}$ exhibits a volcano-shaped dependence on the current densities across all pressure conditions (1–5 bar), with the maximum $FE_{C_2H_4}$ (26.0%) achieved at 0.4 A cm^{-2} under 5 bar (Fig. 5a). This optimal current density (labeled as blue points in Fig. 5b) remains constant regardless of pressure variation, which correlates with the stable interfacial pH profile. Notably, the current density for ethylene production ($j_{C_2H_4}$) plateaus at 118 mA cm^{-2} (5 bar) due to limited C–C coupling capability in bicarbonate media.

In contrast, the KCl system demonstrates pressure-dependent optimization windows (Fig. 5c). While maintaining volcanic trends, the peak positions of $FE_{C_2H_4}$ under fixed pressure shift gradually from 0.4 A cm^{-2} (1 bar) to 1.0 A cm^{-2} (5 bar). This increasing trend of the optimized current density (Δj = 0.6 A cm^{-2} across 1–5 bar) demonstrates strong correlation with interfacial pH change under increasing pressure (Fig. 5d), providing evidence that the interfacial pH change induced by pressure could lead to an inhibited C–C coupling mechanism. Furthermore, this dynamic behavior highlights the critical role of operational parameters on the local reaction environment. Through further optimizing the parameter of current density, the system achieves remarkable performance at 5 bar in KCl electrolyte (Fig. 5e). Notably, faradaic efficiencies of 50% for ethylene and 70% for total C_2 products are obtained at a current density of 1.0 A cm^{-2}, while the ethylene partial current density continues to increase, reaching 554 mA cm^{-2} at 1.2 A cm^{-2}. The KCl based systems exhibit a 5-fold improvement in $j_{C_2H_4}$ (554 *vs.* 118 mA cm^{-2}) relative to bicarbonate-based systems under identical conditions.

In contrast to state-of-the-art high-pressure CO_2RR systems (listed in Table S5),[17,18] which demonstrate promoted formate selectivity under high pressure, this work reveals that pressure induced local pH drop plays a dominant role in decreased C_2 selectivity. Through electrolyte engineering, we alleviated the neutralization effect of the CO_2-derived species. The non-buffered KCl system sustains a pH of >10 (Fig. 5d), which is critical for C–C coupling.[19–21] By adopting low pressure and high current density to preserve the high local pH, this work achieves efficient C_2 selectivity, establishing new benchmarks as shown in the comparative analysis (Fig. 5f and Table S6). Besides, the pressurized L-MEA shows great compatibility with recent pulsed electrolysis[51,52] and ionic liquid additives,[53,54] which highlights its potential for

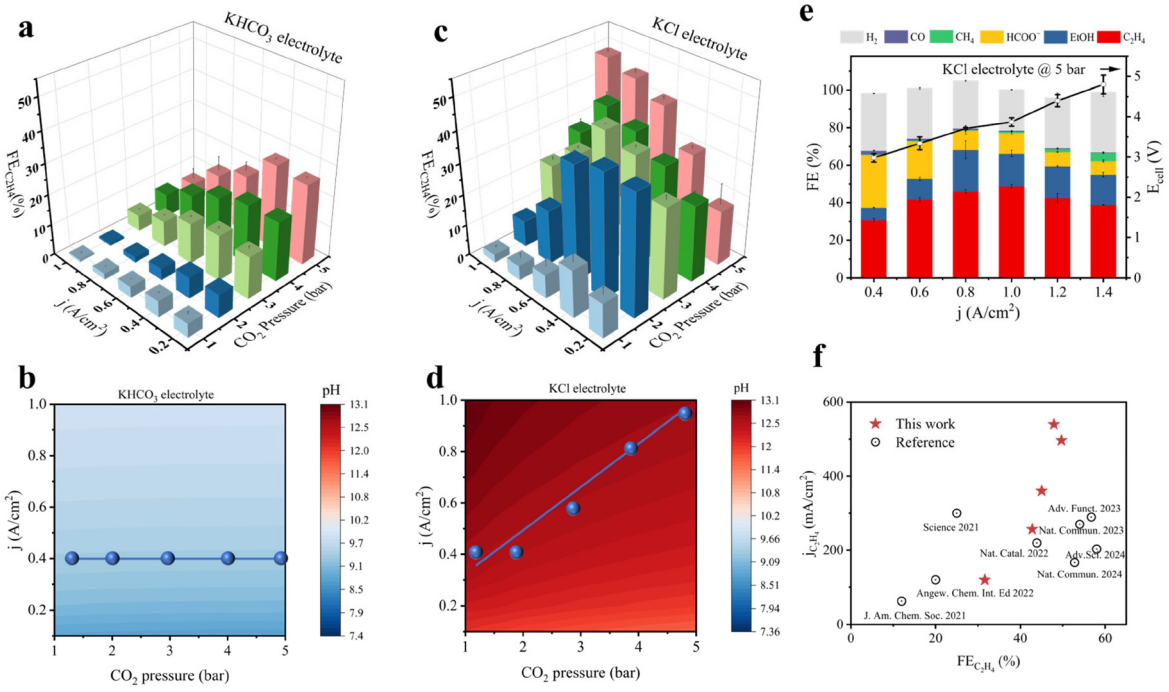

Fig. 5 The influence of CO_2 pressure and current density: (a) the $FE_{C_2H_4}$ and (b) COMSOL simulated interfacial pH at varying CO_2 pressures and current densities in $KHCO_3$ electrolyte; (c) the $FE_{C_2H_4}$ and (d) COMSOL simulated interfacial pH at different CO_2 pressures and current densities in KCl electrolyte; (e) product distribution obtained in KCl electrolyte and CO_2 5 bar; (f) comparison of this work and recent published works (details are listed in Table S5).

synergistic enhancement. Notably, the pressurization energy accounts for less than 0.5% of the total electrolysis energy consumption (Fig. S35–S37), which further supports the energy feasibility of pressurized operations in the context of CO_2 reduction systems.

4. Conclusion

In this work, we present a pressurized CO_2RR system based on an L-MEA and a CuNNA catalyst that utilizes dissolved CO_2 as the reactant under elevated pressure. The enhanced CO_2 accessibility to active sites under pressurized conditions enables ultra-high current densities (0.4–1.0 A cm^{-2}) and selectivity for CO_2RR. Meanwhile, we revealed the buffer effect of both the electrolyte and CO_2 species that significantly decreases the interfacial pH, resulting in hindered C–C coupling. Pressure-dependent experimental and simulation studies further quantitatively elucidated the trade-off between CO_2 concentration and interfacial pH. While higher pressures improve CO_2 availability, they also reduce OH^- concentrations, leading to a performance decline above 2 bar (0.4 A cm^{-2}). By systematically optimizing the electrolyte composition (KCl-based system), pressure (5 bar), and current density (1.0 A cm^{-2}), we achieved a faradaic efficiency of 50% for C_2H_4 and 70% for C_2 products. This represents a 6-fold improvement in the ethylene production rate compared to the conventional bicarbonate systems, highlighting the transformative potential of pressurized operations combined with electrolyte engineering.

Conflicts of interest

There are no conflicts of interest to declare.

Data availability

The data that support the findings of this study are available from the corresponding author upon reasonable request.

Supplementary information is available. See DOI: **https://doi.org/10.1039/d5gc02334c**. Detailed computational methods, density functional theory (DFT), techno-economic analysis, and additional experiment results are included in the supporting information (Figure S1–S37 and Table S1–S5).

Acknowledgements

This work was supported by the National Natural and Science Foundation of China (No. 52394202), the Innovative Research Group Project of the National Natural Science Foundation of China (No. 52021004), the China Postdoctoral Science Foundation (No. BX20240449 and No. 2024M753834), and the Fundamental Research Funds for the Central Universities (No. 2023CDJKYJH084).

References

1 T. O'Carroll, X. Yang, K. J. Gordon, L. Fei and G. Wu, *Adv. Energy Mater.*, 2024, **14**, 2401558.
2 M. G. Kibria, J. P. Edwards, C. M. Gabardo, C. T. Dinh, A. Seifitokaldani, D. Sinton and E. H. Sargent, *Adv. Mater.*, 2019, **31**, 1–24.
3 Q. Wan, L. Yuan, W. Jiang, Y. Liu, L. Zhang, X. Zhuang, J. Zhang and C. Ke, *ACS Sustainable Chem. Eng.*, 2023, **11**, 17046–17052.
4 X. She, L. Zhai, Y. Wang, P. Xiong, M. M.-J. Li, T.-S. Wu, M. C. Wong, X. Guo, Z. Xu, H. Li, H. Xu, Y. Zhu, S. C. E. Tsang and S. P. Lau, *Nat. Energy*, 2024, **9**, 81–91.
5 W. Wu, L. Xu, Q. Lu, J. Sun, Z. Xu, C. Song, J. C. Yu and Y. Wang, *Adv. Mater.*, 2025, **37**, 2312894.
6 W. Fang, W. Guo, R. Lu, Y. Yan, X. Liu, D. Wu, F. M. Li, Y. Zhou, C. He, C. Xia, H. Niu, S. Wang, Y. Liu, Y. Mao, C. Zhang, B. You, Y. Pang, L. Duan, X. Yang, F. Song, T. Zhai, G. Wang, X. Guo, B. Tan, T. Yao, Z. Wang and B. Y. Xia, *Nature*, 2024, **626**, 86–91.
7 S. Hao, A. Elgazzar, N. Ravi, T.-U. Wi, P. Zhu, Y. Feng, Y. Xia, F.-Y. Chen, X. Shan and H. Wang, *Nat. Energy*, 2025, **10**, 26–277.
8 M. Sun, J. Cheng and M. Yamauchi, *Nat. Commun.*, 2024, **15**, 491.
9 Y. Y. Birdja, E. Pérez-Gallent, M. C. Figueiredo, A. J. Göttle, F. Calle-Vallejo and M. T. M. Koper, *Nat. Energy*, 2019, **4**, 732–745.
10 F. Proietto, G. Cammisa, M. Contino, R. Inguanta, A. Galia and O. Scialdone, *ChemSusChem*, 2024, **17**, e202400440.
11 H. Hashiba, S. Yotsuhashi, M. Deguchi and Y. Yamada, *ACS Comb. Sci.*, 2016, **18**, 203–208.
12 J. Li, Y. Kuang, X. Zhang, W.-H. Hung, C.-Y. Chiang, G. Zhu, G. Chen, F. Wang, P. Liang and H. Dai, *Nat. Catal.*, 2023, **6**, 1151–1163.
13 R. Qiu, J. Jia, L. Peng, R. Li, S. Yan, J. Li, J. Zhang, D. T. Sun, Z. Lan, T. Xue, G. Xu, L. Cui, Z. Lv, C. Li, Y. Hong, Y. Guo, B. Ren, S. Yang, J. Li and B. Han, *Green Chem.*, 2023, **25**, 684–691.
14 S. Lamaison, D. Wakerley, J. Blanchard, D. Montero, G. Rousse, D. Mercier, P. Marcus, D. Taverna, D. Giaume, V. Mougel and M. Fontecave, *Joule*, 2020, **4**, 395–406.
15 W. Gao, S. Liang, R. Wang, Q. Jiang, Y. Zhang, Q. Zheng, B. Xie, C. Y. Toe, X. Zhu, J. Wang, L. Huang, Y. Gao, Z. Wang, C. Jo, Q. Wang, L. Wang, Y. Liu, B. Louis, J. Scott, A.-C. Roger, R. Amal, H. He and S.-E. Park, *Chem. Soc. Rev.*, 2020, **49**, 8584–8686.
16 M. C. Freyman, Z. Huang, D. Ravikumar, E. B. Duoss, Y. Li, S. E. Baker, S. H. Pang and J. A. Schaidle, *Joule*, 2023, **7**, 631–651.
17 L. Huang, G. Gao, C. Yang, X.-Y. Li, R. K. Miao, Y. Xue, K. Xie, P. Ou, C. T. Yavuz, Y. Han, G. Magnotti, D. Sinton, E. H. Sargent and X. Lu, *Nat. Commun.*, 2023, **14**, 2958.
18 J. Li, Y. Kuang, Y. Meng, X. Tian, W.-H. Hung, X. Zhang, A. Li, M. Xu, W. Zhou, C.-S. Ku, C.-Y. Chiang, G. Zhu,

J. Guo, X. Sun and H. Dai, *J. Am. Chem. Soc.*, 2020, **142**, 7276–7282.
19 J. E. Huang, F. Li, A. Ozden, A. Sedighian Rasouli, F. P. García De Arquer, S. Liu, S. Zhang, M. Luo, X. Wang, Y. Lum, Y. Xu, K. Bertens, R. K. Miao, C.-T. Dinh, D. Sinton and E. H. Sargent, *Science*, 2021, **372**, 1074–1078.
20 A. Wagner, C. D. Sahm and E. Reisner, *Nat. Catal.*, 2020, **3**, 775–786.
21 F.-Z. Li, H.-G. Qin, H.-L. Zhang, X. Yue, L.-K. Fu, B. Xu, M. Lin and J. Gu, *Joule*, 2024, **8**, 1–18.
22 J. Qu, X. Cao, L. Gao, J. Li, L. Li, Y. Xie, Y. Zhao, J. Zhang, M. Wu and H. Liu, *Nano-Micro Lett.*, 2023, **15**, 178.
23 W. Chen, X. Du, S. Tao, B. Lin, I. Tranca, F. Tielens, M. Ma and Z. Liu, *Chem. Phys. Rev.*, 2025, **6**, 011302.
24 H. Hashiba, L.-C. Weng, Y. Chen, H. K. Sato, S. Yotsuhashi, C. Xiang and A. Z. Weber, *J. Phys. Chem. C*, 2018, **122**, 3719–3726.
25 L. Yang, X. Lv, C. Peng, S. Kong, F. Huang, Y. Tang, L. Zhang and G. Zheng, *ACS Cent. Sci.*, 2023, **9**, 1905–1912.
26 W. Guo, S. Zhang, J. Zhang, H. Wu, Y. Ma, Y. Song, L. Cheng, L. Chang, G. Li, Y. Liu, G. Wei, L. Gan, M. Zhu, S. Xi, X. Wang, B. I. Yakobson, B. Z. Tang and R. Ye, *Nat. Commun.*, 2023, **14**, 7383.
27 P.-P. Yang and M.-R. Gao, *Chem. Soc. Rev.*, 2023, **52**, 4343–4380.
28 X. Yuan, S. Chen, D. Cheng, L. Li, W. Zhu, D. Zhong, Z.-J. Zhao, J. Li, T. Wang and J. Gong, *Angew. Chem., Int. Ed.*, 2021, **60**, 15344–15347.
29 X. Zi, Y. Zhou, L. Zhu, Q. Chen, Y. Tan, X. Wang, M. Sayed, E. Pensa, R. A. Geioushy, K. Liu, J. Fu, E. Cortés and M. Liu, *Angew. Chem., Int. Ed.*, 2023, **62**, e202309351.
30 Z. Zhao, J. Zhang, M. Lei and Y. Lum, *Nano Res. Energy*, 2023, **2**, e9120044.
31 H. Lu, L. Li, Q. Wu, S. Mu, R. Zhao, X. Zheng, C. Long, Q. Li, H. Liu and C. Cui, *ACS Appl. Mater. Interfaces*, 2023, **15**, 13228–13237.
32 Y. Jiang, H. Li, C. Chen, Y. Zheng and S.-Z. Qiao, *ACS Catal.*, 2024, **14**, 8310–8316.
33 Y. Gao, D. Xiao, Z. Wang, Z. Zheng, P. Wang, H. Cheng, Y. Liu, Y. Dai and B. Huang, *Adv. Sci.*, 2024, **11**, 2308949.
34 Y. Gao, Q. Wu, X. Liang, Z. Wang, Z. Zheng, P. Wang, Y. Liu, Y. Dai, M.-H. Whangbo and B. Huang, *Adv. Sci.*, 2020, **7**, 1902820.
35 J. Kim, W. Choi, J. W. Park, C. Kim, M. Kim and H. Song, *J. Am. Chem. Soc.*, 2019, **141**, 6986–6994.
36 Y.-C. Hsieh, S. D. Senanayake, Y. Zhang, W. Xu and D. E. Polyansky, *ACS Catal.*, 2015, **5**, 5349–5356.
37 C. Kang, C. Ding, Y. Li, Y. Li, C. Li and J. He, *Sustainable Energy Fuels*, 2024, **8**, 1730–1739.
38 J. J. Masana, B. Peng, Z. Shuai, M. Qiu and Y. Yu, *J. Mater. Chem. A*, 2022, **10**, 1086–1104.
39 P.-P. Yang, X.-L. Zhang, P. Liu, D. J. Kelly, Z.-Z. Niu, Y. Kong, L. Shi, Y.-R. Zheng, M.-H. Fan, H.-J. Wang and M.-R. Gao, *J. Am. Chem. Soc.*, 2023, **145**, 8714–8725.
40 K. Liu, C. Yang, R. Wei, X. Ma, C. Peng, Z. Liu, Y. Chen, Y. Yan, M. Kan, Y. Yang and G. Zheng, *Sci. Bull.*, 2022, **67**, 1042–1048.
41 Y. Zhou, Y. Liang, J. Fu, K. Liu, Q. Chen, X. Wang, H. Li, L. Zhu, J. Hu, H. Pan, M. Miyauchi, L. Jiang, E. Cortés and M. Liu, *Nano Lett.*, 2022, **22**, 1963–1970.
42 C. Zhan, F. Dattila, C. Rettenmaier, A. Bergmann, S. Kühl, R. García-Muelas, N. López and B. R. Cuenya, *ACS Catal.*, 2021, **11**, 7694–7701.
43 P.-P. Guo, Z.-H. He, S.-Y. Yang, W. Wang, K. Wang, C.-C. Li, Y.-Y. Wei, Z.-T. Liu and B. Han, *Green Chem.*, 2022, **24**, 1527–1533.
44 Z.-Z. Wu, X.-L. Zhang, Z.-Z. Niu, F.-Y. Gao, P.-P. Yang, L.-P. Chi, L. Shi, W.-S. Wei, R. Liu, Z. Chen, S. Hu, X. Zheng and M.-R. Gao, *J. Am. Chem. Soc.*, 2022, **144**, 259–269.
45 Z.-Z. Niu, F.-Y. Gao, X.-L. Zhang, P.-P. Yang, R. Liu, L.-P. Chi, Z.-Z. Wu, S. Qin, X. Yu and M.-R. Gao, *J. Am. Chem. Soc.*, 2021, **143**, 8011–8021.
46 R. Wang, Y. Yang, J. Guo, Q. Zhang, F. Cao, Y. Wang, L. Han and T. Ling, *Nat. Energy*, 2025, **10**, 880–889.
47 A. J. Welch, A. Q. Fenwick, A. Böhme, H.-Y. Chen, I. Sullivan, X. Li, J. S. DuChene, C. Xiang and H. A. Atwater, *J. Phys. Chem. C*, 2021, **125**, 20896–20904.
48 X. Lu, C. Zhu, Z. Wu, J. Xuan, J. S. Francisco and H. Wang, *J. Am. Chem. Soc.*, 2020, **142**, 15438–15444.
49 S. Ma, Y. Kim, Z. Zhang, S. Ren, C. Donde, L. Melo, A. S. R. Williams, M. Stolar, E. R. Grant and C. P. Berlinguette, *ACS Energy Lett.*, 2024, 2326–2332.
50 W. Shan, R. Liu, H. Zhao, Z. He, Y. Lai, S. Li, G. He and J. Liu, *ACS Nano*, 2020, **14**, 11363–11372.
51 J. Wang, Y. Qin, S. Jin, Y. Yang, J. Zhu, X. Li, X. Lv, J. Fu, Z. Hong, Y. Su and H. B. Wu, *J. Am. Chem. Soc.*, 2023, **145**, 26213–26221.
52 X. Wu, X. Li, J. Lv, X. Lv, A. Wu, Z. Qi and H. B. Wu, *Small*, 2024, **20**, 2307637.
53 R. Chen, Q. Wu, J. Zhu, S. Wang, Z. Hu, J. Hu, J. Zhu, H. Zhang, B. Ye, Y. Sun and Y. Xie, *J. Am. Chem. Soc.*, 2025, **147**, 7921–7931.
54 D. Yang, Q. Li, F. Shen, Q. Wang, L. Li, N. Song, Y. Dai and J. Shi, *Electrochim. Acta*, 2016, **189**, 32–37.

